

# A Novel 3D Non-Stationary Massive MIMO Channel Model for Shortwave Communication Systems

Fan Lai<sup>1</sup>, Student Member, IEEE, Cheng-Xiang Wang<sup>2</sup>, Fellow, IEEE, Jie Huang<sup>3</sup>, Member, IEEE, Rui Feng<sup>4</sup>, Xiqi Gao<sup>5</sup>, Fellow, IEEE, and Fu-Chun Zheng<sup>6</sup>, Senior Member, IEEE

**Abstract**—In this paper, a novel three-dimensional (3D) non-stationary massive multiple-input multiple-output (MIMO) channel model for shortwave communication systems is proposed. Three transmission modes, i.e., groundwave, near vertical incident skywave (NVIS), and long-distance skywave are considered to eliminate the blind area and realize the full-coverage for shortwave communication. The ionospheric absorption loss and surface reflection loss during multi-hop transmissions are explored in the proposed channel model. In addition, new massive MIMO channel characteristics including the near-field spherical wavefront effect and spatial non-stationarity are considered. Temporal and frequency non-stationarities are also modeled due to the receiver (Rx) mobility and large relative bandwidth, respectively. The analytical and simulated space cross-correlation function (SCCF), time autocorrelation function (TACF), and frequency correlation function (FCF) of the proposed model are compared. The simulated path loss and singular value spread (SVS) are compared with those of the corresponding channel measurements, illustrating good fittings. In addition, the delay power spectral density (PSD) and Doppler PSD, and channel capacity are also simulated and analyzed. The proposed model can be used as a basis for the design and construction of shortwave communication systems.

**Index Terms**—Shortwave communication, massive MIMO, space-time-frequency non-stationarity, channel model, channel characteristics.

## I. INTRODUCTION

ACCORDING to the international telecommunication union (ITU), shortwave refers to the electromagnetic wave with frequencies ranging from 3–30 MHz. In fact, to make full use of shortwave communications, the frequency range can be expanded to 1.5–30 MHz. Compared with other communication bands, shortwave can realize long-distance transmissions without establishing relay stations. Simple equipment, easy circuit operations, convenient and rapid networks, high flexibility, and strong resistance to natural disasters or wars are main reasons why shortwave communications have been preserved for a long time and are still widely used today [1]. Due to the small number of antennas, conventional shortwave communication systems usually have low transmission data rates, which greatly limits the development of shortwave communications.

Massive multiple-input multiple-output (MIMO) uses a large number of antennas in the base station (BS) side, which can effectively improve the data rate and reliability of communication systems [2]. As a key technology of the fifth generation (5G) and future sixth generation (6G) communication systems [3], massive MIMO has been applied to various frequency bands [4], such as sub-6 GHz [5], [6] and millimeter wave (mmWave) bands. Recently, the application of massive MIMO at shortwave band has been proposed, revealing huge performance gains in comparison with the conventional single-antenna shortwave communications [7]. For example, the massive MIMO skywave radar utilized hundreds of shortwave antennas at both transmitter (Tx) and receiver (Rx) sides [8]. However, the application of massive MIMO in shortwave is difficult due to the much longer wavelength of shortwave, compared with the microwave or mmWave bands. Traditional shortwave systems usually utilized a single antenna or a small number of antennas.

There are three modes of shortwave transmissions, i.e., groundwave, near vertical incident skywave (NVIS), and long-distance skywave [9]. NVIS and long-distance skywave are collectively called the skywave mode. With the groundwave

Manuscript received 29 September 2022; revised 4 March 2023 and 13 May 2023; accepted 16 May 2023. Date of publication 1 June 2023; date of current version 18 September 2023. This work was supported by the National Key R&D Program of China under Grants 2020YFB1805005, the National Natural Science Foundation of China (NSFC) under Grants 61960206006 and 62271147, the Key Technologies R&D Program of Jiangsu (Prospective and Key Technologies for Industry) under Grants BE2022067, BE2022067-1, BE2022067-2, and BE2022067-5, the EU H2020 RISE TESTBED2 project under Grant 872172, the High Level Innovation and Entrepreneurial Doctor Introduction Program in Jiangsu under Grant JSSCBS20210082, the Start-up Research Fund of Southeast University under Grant RF1028623029, the Fundamental Research Funds for the Central Universities under Grant 2242023K5003, and the Shenzhen Science and Technology Program under Grant KQTD20190929172545139. The associate editor coordinating the review of this article and approving it for publication was N. Miridakis. (Corresponding authors: Cheng-Xiang Wang; Fu-Chun Zheng.)

Fan Lai, Cheng-Xiang Wang, Jie Huang, Rui Feng, and Xiqi Gao are with the National Mobile Communications Research Laboratory, School of Information Science and Engineering, Southeast University, Nanjing 210096, China, and also with Purple Mountain Laboratories, Nanjing 211111, China (e-mail: lai\_fan@seu.edu.cn; chxwang@seu.edu.cn; j\_huang@seu.edu.cn; fengrui@pmlabs.com.cn; xqgao@seu.edu.cn).

Fu-Chun Zheng is with the School of Electronic and Information Engineering, Harbin Institute of Technology (Shenzhen), Shenzhen 518055, China, and also with the National Mobile Communications Research Laboratory, Southeast University, Nanjing 210096, China (e-mail: fzheng@ieee.org).

Color versions of one or more figures in this article are available at <https://doi.org/10.1109/TCOMM.2023.3281875>.

Digital Object Identifier 10.1109/TCOMM.2023.3281875

0090-6778 © 2023 IEEE. Personal use is permitted, but republication/redistribution requires IEEE permission. See <https://www.ieee.org/publications/rights/index.html> for more information.

transmission, radio waves propagate along the earth surface [10]. The transmission performance is mainly affected by the distribution density of surface radio waves. The energy of shortwave signals will be gradually absorbed by the surface, until they are seriously attenuated and cannot be recognized by the Rx. The skywave propagates relying on the ionosphere. Radio waves generated by Tx antennas reach the ground after multi-stage reflections and refractions through the ionosphere and are captured by the Rx to achieve data recovery. With the special property of atmospheric ionosphere, shortwave signals can reach thousands of kilometers for data transmissions. Radio waves of NVIS travel in a nearly vertical elevation angle into the ionosphere in order to transmit the signal at a shorter distance than the long-distance skywave.

The research of channel model is the foundation of communication research [11] and is very important for theoretical analysis, performance evaluation [12]. In 1965, Watterson et al. measured some typical ionospheric channels and proposed the Watterson model based on the measurement data. Watterson model [13] was recommended as an ITU standard model to describe shortwave channels. In 1987, Martin proposed a modeling method for shortwave wideband channels based on the Watterson model [14]. In 1987, Barratt et al. proposed an improved Watterson wideband channel model [15]. Both models use the tapped delay line structure to model time-varying channel transmission functions. In 1997, L. Van der Perre et al. implemented a shortwave wideband channel simulator [16] by means of multi-channel digital signal processing (DSP), based on the extended Watterson model. The simulator processes signals in the frequency domain and decomposes wideband signals into several sub-frequency bands. In 2000, Milson proposed a shortwave wideband channel model suitable for short-range communications [17]. In this model, the internal dispersion of the model adopted a Gaussian distribution shape. The output was connected with a filter with parabolic phase response and flat amplitude response to achieve the group delay characteristics of the channel. With multiple DSPs, this method was realized in the time domain simulation of shortwave wideband channel.

In 1988, Vogler and Hoffmeyer [18] proposed a shortwave wideband channel modeling method based on ionospheric parameters, namely ionospheric parameters model (IPM). Based on the channel scattering function, Vogler and Hoffmeyer completed the IPM model in 1990. The deterministic and stochastic parts of IPM model were studied in [19]. A large number of channel scattering function data from Basler test in 1987 [20] was used to simulate, compare, and verify the model accuracy. Authors in [21], [22] studied the hardware implementation method of the model, and considered the noise and interference in the shortwave channel [23], [24], [25]. In 1997, the Institute for Telecommunication Sciences (ITS) implemented a shortwave wideband channel simulator using DSP [26], which was based on the IPM model. The channel impulse response (CIR) of the ITS model was further expressed in three parts, i.e., power delay profile, deterministic phase function, and random modulation function. The ITS model was often used for simulations and applied to narrowband and wideband channels. The ITS model was also used

to characterize the noise and interference of the channel [27]. Authors in [28] simulated the ITS model under narrowband conditions. Based on this model, channel characteristics were studied in [29], such as correlation bandwidth and correlation time, which are critical to the shortwave communication system design.

In recent years, geometry-based statistic models (GBSMs) have been widely used to model the real channels using the geometric relationship for the antenna arrays, scatterers, and clusters. A three-dimensional (3D) massive MIMO channel model was first proposed by authors in [30]. Clusters for the real environments were modeled as the twin-cluster framework and spatial-temporal (ST) non-stationarities were also included. Lopez et al. [31] proposed a 3D WINNER-like massive MIMO channel model based on an approximation algorithm for calculating spherical wavefront, i.e., parabolic wavefront. Another WINNER-type massive MIMO channel model was proposed by Martinez et al. [32], where authors utilized a two-state Markov process to model the spatial non-stationarity. Xie et al. [33] proposed a 3D two-cylinder massive MIMO channel model by modeling the spatial non-stationarity with a 3D visible area. The GBSM is also used in several standardized channel models, such as NYU WIRELESS [34], 3rd Generation Partnership Project (3GPP) 38.901 [35], and METIS [36]. However, those shortwave channel models mentioned above are all non-geometry-based stochastic channel models (non-GBSMs). In addition, most of these models do not support massive MIMO under shortwave bands. In addition, most of these channel models support a single shortwave propagation mode. Thus, to increase the data rate, a general massive MIMO shortwave channel model that can be used in three transmission modes is needed. To fill this gap, we propose a novel three-dimensional (3D) non-stationary GBSM for shortwave communication systems in this paper. The main contributions and novelties of this paper are as follows.

- 1) A novel 3D non-stationary massive MIMO GBSM containing three propagation modes, i.e., groundwave, NVIS, and long-distance skywave, is proposed for shortwave communication systems. The frequency prediction method according to ITU is introduced to predict the optimal working frequency (OWF). The ionospheric absorption loss and surface reflection loss during multi-hop transmission are employed in the proposed channel model.
- 2) Specific massive MIMO characteristics are introduced into the novel shortwave channel model for the first time, including the near-field spherical wavefront and spatial non-stationarity. Temporal and frequency non-stationarities are also modeled due to the continuous movement of Rx and large relative bandwidth, respectively.
- 3) Statistical characteristics of the proposed channel model, including STF correlation functions (STFCFs), are derived and simulated. The path loss and singular value spread (SVS) are simulated and compared with the measurement data to verify the accuracy of the proposed model. In addition, the delay power spectral density

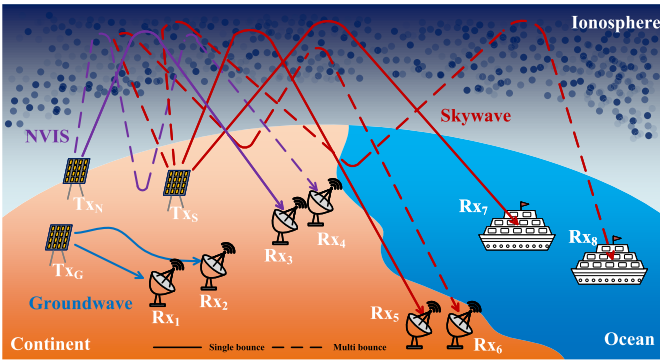


Fig. 1. Three propagation modes for shortwave communications.

(PSD), Doppler PSD, and channel capacity are also simulated and analyzed.

The remainder of this paper is organized as follows. The proposed novel shortwave massive MIMO channel model is presented in Section II. In Section III, the derivation of channel statistical properties is presented. Section IV shows the results and analysis. Finally, conclusions are drawn in Section V.

## II. THE PROPOSED SHORTWAVE MASSIVE MIMO GBSM

As shown in Fig. 1, shortwave communications have three propagation modes: the groundwave, NVIS, and long-distance skywave modes. When adopting the skywave mode, the electromagnetic waves need to pass through the ionosphere and the ionospheric absorption effect should be considered. Meanwhile, the ground reflection effect should be taken into account when we utilize groundwave transmissions. The transmission distance of groundwave is generally less than 150 km [10], while the transmission distance of long-distance skywave is more than 300 km [1]. This may lead to a communication blind area between the groundwave and long-distance skywave modes. In order to solve this problem, the NVIS mode is introduced, which transmits electromagnetic waves through the near-vertical incident angle and propagates via the skywave. The propagation distance of NVIS is about 150–300 km, which is enough to cover the communication dead zone between the groundwave and long-distance skywave modes. The cooperation of three modes can realize the full coverage of shortwave communications.

### A. Communication Distances of Three Shortwave Communication Modes

#### 1) Maximum Communication Distance of Groundwave:

Groundwave propagation can be divided into the direct wave mode and surface wave mode. The direct wave, also known as space wave, propagates from space straight line to the Rx. The surface wave propagates along the earth surface to the Rx. The limit distance of groundwave propagation is determined by the maximum transmission distance of two modes.

The propagation distance of direct wave is generally limited to the visual range. The line-of-sight (LOS) propagation of radio waves is affected by the radius of curvature of the earth. The relationship between the limit direct distance and the

height of transmitting and receiving antennas can be expressed as [37]

$$D_{\text{direct}} = 3.57 \left( \sqrt{h_T} + \sqrt{h_R} \right) \quad (1)$$

where  $D_{\text{direct}}$  is in the unit of km. The height of transmitting and receiving antennas are denoted as  $h_T$  and  $h_R$  with the unit of m, respectively. Considering the refraction of atmosphere on the radio wave, the effective propagation distance of direct wave is [37]

$$D_{\text{direct}}^{\text{eff}} = 2.884 \left( \sqrt{h_T} + \sqrt{h_R} \right). \quad (2)$$

Surface waves are radio waves that travel along the boundary between earth and air. The propagation distance of surface waves is related with the dielectric coefficient  $\epsilon$ , electrical conductivity  $\sigma$ , and the permeability  $\mu$  of the ground. Different ground media leads to different loss in waves. The attenuation of moist-soil ground is small, while that of dry-sand ground is large. At the same time, surface wave attenuation is also associated with radio frequency. The high frequency leads to the great attenuation. It is relatively stable with small dispersion effect because the geomorphology, ground objects, and soil electrical parameters do not change quickly with time and are not affected by meteorological conditions. The propagation distance of surface wave with the unit of km can be expressed as

$$D_{\text{surface}} = 80 f_c^{-\frac{1}{3}} \quad (3)$$

where the working frequency of shortwave communication systems is denoted as  $f_c$  with the unit of MHz. Therefore, the maximum communication distance of groundwave is

$$D_{\text{max}}^G = \max \{ D_{\text{direct}}^{\text{eff}}, D_{\text{surface}} \}. \quad (4)$$

2) *Minimum Communication Distance of Long-Distance Skywave:* The transmitted shortwave signal is reflected by the ionosphere back to the ground, and reflected by ground back into the ionosphere. Reflection repeats several times, and thus the signal can spread an extremely long distance (hundreds to thousands of kilometers). The propagation is not affected by the ground obstacle blocking. However, the path loss, time delay, atmospheric noise, multipath effect, and ionospheric attenuation will weaken or distort the signal.

The propagation distance of long-distance skywave is related to radio frequency, ionosphere state, and incident angle. According to measurement results, the change of electron concentration near the maximum ionospheric ionization position can be expressed as

$$N(Z) = N_{\text{max}} \left[ 1 - \left( \frac{Z_m - Z}{Z_m} \right)^2 \right] \quad (5)$$

where  $N_{\text{max}}$  is the maximum ionization concentration,  $Z$  denotes the height, and  $Z_m$  represents the height from the bottom of the ionosphere to the maximum electron concentration position. According to the distribution law of electron concentration in (6), the minimum communication distance with the unit of km of long-distance skywave is

$$D_{\text{min}}^S = D_1 + D_2. \quad (6)$$

Parameters  $D_1$  and  $D_2$  are denoted as

$$D_1 = \alpha\beta R_E \sin \theta_0 \cdot \ln \left[ \frac{\alpha + \cos \theta_0 - \alpha\beta \sin^2 \theta_0}{\alpha - \cos \theta_0 - \alpha\beta \sin^2 \theta_0} \right] \quad (7)$$

$$D_2 \cong 2R_E \left[ \text{ctg} \theta_0 - \sqrt{\text{ctg}^2 \theta_0 - (2h_I/R_E)} \right]. \quad (8)$$

Here,  $\theta_0$  is the incident angle of electromagnetic wave,  $\alpha = f_c/f_b$ , and  $\beta = Z_m/(R_E + h_I)$ . The boundary frequency is  $f_b = \sqrt{80.0 N_{\max}}$ , the earth radius is  $R_E$ , and the height of ionosphere is  $h_I$ . The cotangent operation is denoted as  $\text{ctg}(\cdot)$ .

3) *Switching of Three Modes for Shortwave Communications*: According to the above calculations, we achieve the maximum distance of groundwave mode and the minimum distance of long-distance skywave mode. The area between two distances is the shortwave communication dead zone. To eliminate this blind spot, NVIS mode is introduced. Assume that  $D$  is the transmission distance between the Tx and Rx, we can divide these three modes as follows.

- When  $D \leq D_{\max}^G$ , the groundwave mode will be utilized.
- When  $D_{\max}^G < D < D_{\min}^S$ , the NVIS mode will be utilized.
- When  $D \geq D_{\min}^S$ , the long-distance skywave mode will be utilized.

In general, reference values of  $D_{\max}^G$  and  $D_{\min}^S$  are 150 km and 300 km.

### B. Frequency Prediction Method

Recommendation ITU-R P.373 [38] provides definitions of maximum and minimum transmission frequencies. Following definitions are used for this paper.

- *Operational maximum usable frequency (MUF)* is the highest frequency where signals propagate through the ionosphere between specified terminals under specified operating conditions and at specified times, giving a radio circuit acceptable performance.
- *Basic MUF* is the highest frequency where radio waves travel between particular terminals on a particular occasion and refracted only by the ionosphere.
- *Optimum working frequency (OWF)* is the lower tenth of the operational MUF daily value for a given period of time (usually a month).

According to the change of electron density with height, the ionosphere can be divided into D-layer, E-layer, F1-layer, and F2-layer, as depicted in Fig. 2. F2-layer has the highest electron density and D-layer has the lowest electron density. The specific forecast method according to Recommendations ITU-R P.533 [39] and ITU-R P.1240 [40] is briefly described here.

1) *Calculation of MUFs*: When calculating the basic MUF, the reflection layers for the radio wave propagation include E-, F1-, and F2-layers. Thus, calculations of the basic MUF for the above three ionospheric layers are introduced here. There is no basic MUF in the D-layer. The basic MUF of E-layer with the unit of MHz can be calculated as

$$\text{MUF}_E = M_E \cdot f_E. \quad (9)$$

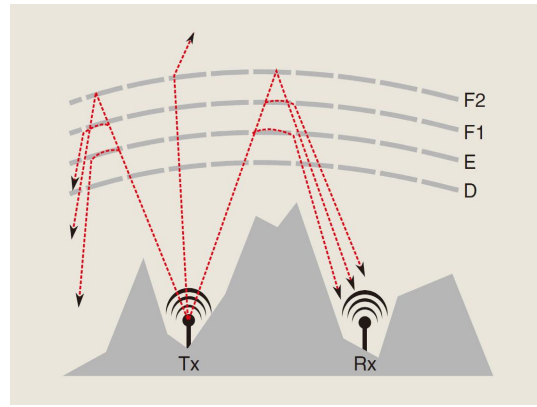


Fig. 2. Illustration of different ionospheric layers [9].

The critical frequency of the E-layer at the midpoint of the path is  $f_E$  and the parameter  $M_E$  can be further derived as

$$M_E = 3.94 + 2.80\omega - 1.70\omega^2 - 0.60\omega^3 + 0.96\omega^4 \quad (10)$$

$$\omega = \min(D/1150 - 1, 0.74). \quad (11)$$

Basic MUF of F1-layer with the unit of MHz can be calculated as

$$\text{MUF}_{F1} = M_{F1} \cdot f_{F1}. \quad (12)$$

The critical frequency of the F1-layer at the midpoint of the path is represented as  $f_{F1}$  and the parameter  $M_{F1}$  can be further derived as

$$M_{F1} = K_0 - 0.01(K_0 - K_{100})R_{12} \quad (13)$$

$$K_0 = 0.16 + 2.64 \times 10^{-3}D - 0.40 \times 10^{-6}D^2 \quad (14)$$

$$K_{100} = -0.52 + 2.69 \times 10^{-3}D - 0.39 \times 10^{-6}D^2. \quad (15)$$

For the propagation of F2-layer,  $D_{F2}^{\max}$  represents the maximum hop length calculated at the mid-path control point. Basic MUF of F2-layer with the unit of MHz can be expressed as

$$\text{MUF}_{F2} = [1 + (S_D/S_{3000})(B - 1)] f_{F2} + f_{MR}(1 - D_n/D_{\max})/2 \quad (16)$$

where

$$B = J_{F2} - 0.124 + (J_{F2}^2 - 4) \times \left[ 0.0215 + 0.005 \sin \left( \frac{7.854}{\max(f_{F2}/f_E, 2)} - 1.9635 \right) \right] \quad (17)$$

$$S_D = 0.74 - 0.591Z - 0.424Z^2 - 0.090Z^3 + 0.088Z^4 + 0.181Z^5 + 0.096Z^6 \quad (18)$$

$$Z = 1 - 2D_n/D_{F2}^{\max} \quad (19)$$

$$D_n = D/n_0. \quad (20)$$

Here,  $J_{F2}$  is transmission factor of  $\text{MUF}_{F2}$  at midpoint of path,  $S_{3000}$  is the  $S_D$  value at  $D = 3000$  km,  $n_0$  is the minimum hop propagation at F2-layer,  $f_{F2}$  is the critical frequency value at F2-layer at the midpoint of the path, and  $f_{MR}$  is the magnetic rotation frequency at the midpoint of the

TABLE I  
THE RATIO  $R_{op}$  OF WORKING MUF AND BASIC MUF AT F2-LAYER [40]

Power (dBW)	Summer		Spring & Autumn		Winter	
	Nighttime	Daytime	Nighttime	Daytime	Nighttime	Daytime
$\leq 30$	1.20	1.10	1.25	1.15	1.30	1.20
$> 30$	1.25	1.15	1.30	1.20	1.35	1.25

path. In summary, the highest available working frequency can be obtained as

$$\text{MUF} = \max(\text{MUF}_E, \text{MUF}_{F1}, \text{MUF}_{F2} \cdot R_{op}) \quad (21)$$

where  $R_{op}$  is the ratio of working MUF and basic MUF at F2-layer. Values of  $R_{op}$  for different cases are shown in Table I.

2) *Calculation of OWFs*: Based on calculations above, the basic MUF of each layer is obtained, and the MUF-OWF conversion factor ( $F_l$ ) is used to obtain the OWF, which can be expressed as

$$\text{OWF} = \max(\text{OWF}_E, \text{OWF}_{F1}, \text{OWF}_{F2}). \quad (22)$$

Here,  $\text{OWF}_E$ ,  $\text{OWF}_{F1}$ , and  $\text{OWF}_{F2}$  are represented as the OWFs at E-, F1-, and F2-layer, respectively. They can be further expressed as

$$\text{OWF}_E = 0.95 \cdot \text{MUF}_E \quad (23)$$

$$\text{OWF}_{F1} = 0.95 \cdot \text{MUF}_{F1} \quad (24)$$

$$\text{OWF}_{F2} = R_{op} \cdot \text{MUF}_{F2} \cdot F_l \quad (25)$$

where  $F_l$  is the MUF-OWF conversion factor.

### C. Channel Matrix

The shortwave channel matrix  $\mathbf{H}$  is composed of three propagation modes

$$\mathbf{H} = \mathbf{H}^G \cdot \varepsilon(D_{\max}^G - D) + \mathbf{H}^N \cdot \varepsilon(D - D_{\max}^G) \cdot \varepsilon(D_{\min}^S - D) + \mathbf{H}^S \cdot \varepsilon(D - D_{\min}^S). \quad (26)$$

Here,  $\mathbf{H}$  is a  $M_R \times M_T$  matrix, where  $M_T$  and  $M_R$  denote numbers of Tx and Rx antennas, respectively.  $\mathbf{H}^G$ ,  $\mathbf{H}^N$ , and  $\mathbf{H}^S$  represent channel matrices for the groundwave, NVIS, and long-distance skywave modes, respectively. The function  $\varepsilon(\cdot)$  is a unit step function, which can be denoted as

$$\varepsilon(x) = \begin{cases} 1, & x \geq 0 \\ 0, & x < 0. \end{cases} \quad (27)$$

Considering path loss, shadowing, and small-scale fading, the complete channel matrix is given by

$$\mathbf{H}^P = \sqrt{PL^P \cdot SH^P} \cdot \mathbf{H}_S^P \quad (28)$$

where  $P \in \{G, N, S\}$  and  $\mathbf{H}_S^P$  is the channel matrix of small-scale fading. The path loss is represented as  $PL$  and shadowing is denoted as  $SH$ .

1) *Path Loss*: For the groundwave mode, assuming the propagation path is far away from the ground and there is no obstruction, the influence of air can be ignored. Short-wave can be approximately considered to propagate in free space and thus the propagation model for radio wave in free space is adopted. Some empirical formulas and models are often adopted in engineering. Okumura-Hata model is one of empirical models used in shortwave wireless mobile communications. Main suitable environments and conditions of this model are quasi-flat areas in small towns and suburbs. Hata distilled the Okumura model's experience curves and charts into a more easily usable empirical formula, known as the Okumura-Hata empirical formula. The path loss for the groundwave mode with the unit of dB can be expressed as [41]

$$PL^G = 69.55 + 26.16 \lg f_c - 13.82 \lg h_T - \alpha(h_R) + (44.9 - 6.55 \lg h_T) \lg D - C \quad (29)$$

where  $C$  is the modified coefficient of the communication environment, and  $\alpha(\cdot)$  is the modified factor. Since the original Okumura-Hata model is limited, it can no longer meet the complex battlefield electromagnetic environment of shortwave communications. The model is modified by using electromagnetic field simulation technology. The modified Okumura-Hata model [41] can be calculated as

$$PL_{\text{mod}}^G = 147.15 + 18.93 \lg f_c - 6.68 \lg h_T - \alpha(h_R) + (44.9 - 6.55 \lg h_T) \lg D \quad (30)$$

$$\alpha(h_R) = (1.1 \lg f_c - 0.7)h_R - (1.56 \lg f_c - 0.8). \quad (31)$$

For NVIS and long-distance skywave modes, the path loss  $PL^{N/S}$  with the unit of dB can be divided into three parts [42].

$$PL^{N/S} = L_f + L_i + L_r. \quad (32)$$

Here, the first item  $L_f$  is the basic transmission loss in free space. The second item  $L_i$  is the ionospheric absorption loss. The third item  $L_r$  is the reflection loss caused by the ground or sea surface reflection during multi-hop transmission. The basic transmission loss  $L_f$  of skywave propagation can be expressed as

$$L_f = 32.45 + 20 \lg f_c + 20 \lg D. \quad (33)$$

Ionospheric absorption loss  $L_i$  includes offset absorption loss and non-offset absorption loss. The offset absorption is generally less than 1 dB and often ignored. The calculation of non-offset absorption is very complicated and a semi-empirical formula is often used in engineering calculation. The formula is expressed as

$$L_i = \frac{677.2 N_H I_a \sec \theta_{100}}{(f_c + f_{100})^{1.98} + 10.2} \quad (34)$$

where  $N_H$  is the number of path hops,  $I_a$  is the absorption index,  $\theta_{100}$  is the incidence angle at the height of 100 km, and  $f_{100}$  (MHz) is the gyromagnetic frequency at the height of 100 km. The absorption index  $I_a$  can be further calculated as

$$I_a = (1 + 0.037 N_S)[\cos(0.881\chi)]^{1.3}. \quad (35)$$

Here,  $N_S$  is the average number of sunspots in 12 months and  $\chi$  is solar zenith angle. The reflection loss  $L_r$  is given by

$$L_r = 10 \lg \left( \frac{|R_v|^2 + |R_h|^2}{2} \right). \quad (36)$$

The corresponding parameters in the above equation can be calculated by

$$R_v = \frac{n^2 \sin \theta_e - (n^2 - \cos^2 \theta_e)^{\frac{1}{2}}}{n^2 \sin \theta_e + (n^2 - \cos^2 \theta_e)^{\frac{1}{2}}} \quad (37)$$

$$R_h = \frac{\sin \theta_e - (n^2 - \cos^2 \theta_e)^{\frac{1}{2}}}{\sin \theta_e + (n^2 - \cos^2 \theta_e)^{\frac{1}{2}}} \quad (38)$$

$$n^2 = \epsilon - j(1.8 \times 10^4) \frac{\sigma}{f_c} \quad (39)$$

where the elevation angle is denoted as  $\theta_e$ .

2) *Shadowing*: In rural areas, for all paths of a given length, following equations can be used to estimate the standard variance  $\sigma_L$  (dB) of their distribution [43].

$$\sigma_L = \begin{cases} 6 + 0.69\sqrt{\Delta h/\lambda} - 0.0063(\Delta h/\lambda), & \Delta h/\lambda < 3000 \\ 25, & \Delta h/\lambda \geq 3000 \end{cases} \quad (40)$$

where  $\Delta h$  is the interdecile height variation and  $\lambda$  is the wavelength. In flat urban areas, the standard deviation over a large area can be estimated by

$$\sigma_L = 5.25 + 0.42 \log(f_c/100) + 1.01 \log^2(f_c/100). \quad (41)$$

Here, the standard deviation is valid from 3–30 MHz. Some measurement results for all types of land cover within 50 km are summarized as [43]

$$\sigma_L = 2.7 + 0.42 \log(f_c/100) + 1.01 \log^2(f_c/100). \quad (42)$$

3) *Small-Scale Fading*: For small-scale fading, the scattering cluster distribution needs to be paid more attention. Clusters of a shortwave channel refer to the aggregated scatterers near the Tx and Rx sides. The twin-cluster wideband channel model is therefore necessary, and the difference from the previous terrestrial twin-cluster model is the long propagation path, including land, sea, air, and other complex environments, between clusters at the Tx side and clusters at the Rx side. For the long path with these complex situations, we have abstracted it into a virtual link in the model. Due to the long distance, such a virtual link is dominated by large-scale fading and hardly impacted by small-scale parameters. The large-scale fading of the proposed model is considered and described above, including the ionospheric absorption and ground surface (sea surface) reflection fading.

Especially for long-distance skywave communications, due to the introduction of massive MIMO, we should consider

the corresponding channel characteristics, such as the near-field spherical wavefront effect and spatial non-stationarity. In addition, the temporal and frequency non-stationarities are also needed to be study. Therefore, compared with traditional shortwave channel models, the accurate small-scale fading model for long-distance skywave needs to be rebuilt.

The illustration of channel models for three propagation modes is shown in the Fig. 3. The shortwave channel is a multipath fading channel. The whole shortwave channel is formed by superimposing the multipath channel according to the geometric relationship, which is consistent with the pervasive channel modeling idea. The small-scale fading components of the proposed channel model is based on the beyond 5G (B5G) general channel model [44] and 6G pervasive channel model (6GPCM) framework [45]. Elements of the small-scale channel matrix are represented as  $[\mathbf{H}_S^P(t, \tau)]_{qp} = h_{qp}^P(t, \tau)$ , where  $P \in \{G, N, S\}$  and  $q/p = 1, 2, \dots, M_R/M_T$ . The CIR  $h_{qp}^P(t, \tau)$  can be further calculated as (43), shown at the bottom of the next page. Antenna patterns of vertical and horizontal polarization for the  $p$ -th transmit antenna and the  $q$ -th receive antenna are represented as  $F_{p(q),V}^P$  and  $F_{p(q),H}^P$ , respectively. Angles  $\theta_{m_n}^{VV}, \theta_{m_n}^{VH}, \theta_{m_n}^{HV}$ , and  $\theta_{m_n}^{HH}$  follow the uniform distribution over  $(0, 2\pi]$ . The cross polarization power ratio is denoted by  $\kappa_{m_n}$  [35]. Powers of the  $m$ -th ray in the  $n$ -th cluster between  $A_p^T$  and  $A_q^R$  at time  $t$  are represented as  $P_{qp,m_n}^P(t)$ . Delays of the  $m$ -th ray in the  $n$ -th cluster between  $A_p^T$  and  $A_q^R$  at time  $t$  are denoted as  $\tau_{qp,m_n}^P(t)$ . The carrier frequency  $f_c^P$  will be obtained by calculating the OWF using the frequency prediction method in Section II-B. Delay parameter  $\tau_{qp,m_n}^P(t)$  calculated as

$$\tau_{qp,m_n}^P(t) = d_{qp,m_n}^P(t)/c + \tilde{\tau}_{m_n}^P \quad (44)$$

where  $c$  represents the light velocity and  $\tilde{\tau}_{m_n}^P$  denotes the delay of the link between  $S_{m_n}^A$  and  $S_{m_n}^Z$ .

$$\tilde{\tau}_{m_n}^P = \tilde{d}_{m_n}^P/c + \tau_{C,\text{link}}^P. \quad (45)$$

In (46),  $\tilde{d}_{m_n}^P$  is the length between two scatterers and  $\tau_{C,\text{link}}^P$  follows non-negative exponential distribution. The distance parameter  $d_{qp,m_n}^P(t)$  is denoted as

$$d_{qp,m_n}^P(t) = \left\| \vec{d}_{p,m_n}^T(t) \right\| + \left\| \vec{d}_{m_n,q}^R(t) \right\|. \quad (46)$$

Here,  $\|\cdot\|$  represents the Frobenius norm,  $\vec{d}_{p,m_n}^T(t)$  and  $\vec{d}_{m_n,q}^R(t)$  are two distance vectors from  $A_p^T$  to  $S_{m_n}^A$  and from  $A_q^R$  to  $S_{m_n}^Z$  at time  $t$ , respectively. The vector  $\vec{d}_{p,m_n}^T(t)$  is calculated as

$$\vec{d}_{p,m_n}^T(t) = \vec{d}_{m_n}^T - \left[ \vec{l}_p^T + \int_0^t \vec{v}^T(t) - \vec{v}^{A_n}(t) dt \right] \quad (47)$$

where  $\vec{d}_{m_n}^T$  denotes the distance vector from  $A_1^T$  to  $C_n^A$  via the  $m$ -th ray at the initial time. The distance vector from  $A_p^T$  to  $A_1^T$  is represented as  $\vec{l}_p^T$ . The velocity vectors of the Tx and  $C_n^A$  are denoted as  $\vec{v}^T(t)$  and  $\vec{v}^{A_n}(t)$ , respectively.

$$\vec{d}_{m_n}^T = d_{m_n}^T \left[ \cos(\phi_{E,m_n}^T) \cos(\phi_{A,m_n}^T), \right. \\ \left. \cos(\phi_{E,m_n}^T) \sin(\phi_{A,m_n}^T), \sin(\phi_{E,m_n}^T) \right] \quad (48)$$



We adopt the von Mises Fisher (VMF) distribution to jointly consider the impact of azimuth and elevation angles on channel statistics model angular parameters  $\alpha_n^T$ ,  $\beta_n^T$ ,  $\alpha_n^R$ , and  $\beta_n^R$  of Cluster<sub>*n*</sub>.

$$f(\alpha_n^T, \beta_n^T) = \frac{k \cos \beta}{4\pi \sinh k} e^{k[\cos \beta_0 \cos \beta \cos(\alpha - \alpha_0) + \sin \beta_0 \sin \beta]} \quad (56)$$

In (57),  $\alpha, \beta \in [-\pi, \pi)$ . Mean values of the azimuth angle  $\alpha$  and elevation angle  $\beta$  can be denoted as  $\alpha_0$  and  $\beta_0$ , respectively. Parameter  $k$  ( $k \geq 0$ ) is real-valued. The mean power of  $m_n$  rays within cluster<sub>*n*</sub> can be modeled as

$$P'_{n,m_n} = e^{-\frac{\tau m_n (r_r - 1)}{\mathbb{E}[\tau m_n]}} \cdot 10^{-\frac{Z_{n,m_n}}{10}} \quad (57)$$

where  $Z_{n,m_n}$  is the shadowing following the Gaussian distribution. The mean power of rays can be normalized as

$$P_{n,m_n} = P_n \cdot \frac{P'_{n,m_n}}{\sum_{m_n=1}^{M_n} P'_{n,m_n}} \quad (58)$$

### E. STF Cluster Evolution

Based on the birth-death process, the STF cluster evolution is proposed for the shortwave channel model. Generation and recombination rates of clusters are  $\lambda_G$  and  $\lambda_R$ , respectively. Survival probabilities of clusters  $P_{\text{survival}}^T$  and  $P_{\text{survival}}^R$  are denoted as

$$P_{\text{survival}}^T = e^{-\lambda_R \frac{\delta_T}{D_c^a}} \quad (59)$$

$$P_{\text{survival}}^R = e^{-\lambda_R \frac{\delta_R}{D_c^a}} \quad (60)$$

where  $D_c^a$  is the array scenario-dependent correlation factor. Then, the STF cluster evolution process is illustrated in Fig. 4 and shown as follows.

Step 1.

- 1) We generate initial clusters at time  $t$ , and randomly distributed parameters, such as number of rays, delays, power, angular parameters, and virtual link delay.
- 2) At time  $t + \Delta t$ , two possible situations may happen, and then we discuss them separately. When  $t$  is divisible by  $\Delta t_M$ , the mean relative velocities  $\Delta v_n^R$  and  $\Delta v_n^T$  are characterized as  $\Delta v_n^R = \mathbb{E}[\|\mathbf{v}_n^R\|]$  and  $\Delta v_n^T = \mathbb{E}[\|\mathbf{v}_n^T\|]$ , respectively. Then, the survival probability  $Pr(\Delta t)$  of a cluster after  $\Delta t$  is denoted as

$$Pr(\Delta t) = e^{-\lambda_R \frac{P_F (\Delta v_n^R + \Delta v_n^T) \Delta t}{D_i^s}} \quad (61)$$

where  $P_F$  is the percentage of moving clusters and  $D_i^s$  is a scenario-dependent coefficient describing space correlation. The survival probability of each cluster at time  $t + \Delta t$  is  $Pr(\Delta t)$ . Due to the relatively large bandwidth of shortwave communication systems, the frequency non-stationarity of shortwave channels should be considered. To this end, we divide the whole bandwidth into different sub-bands, and the cluster evolution over different sub-bands along the frequency axis is modeled by a birth-death process. Then the cluster evolution on the frequency axis can be operated in a similar manner to cluster evolution on the time axis. The

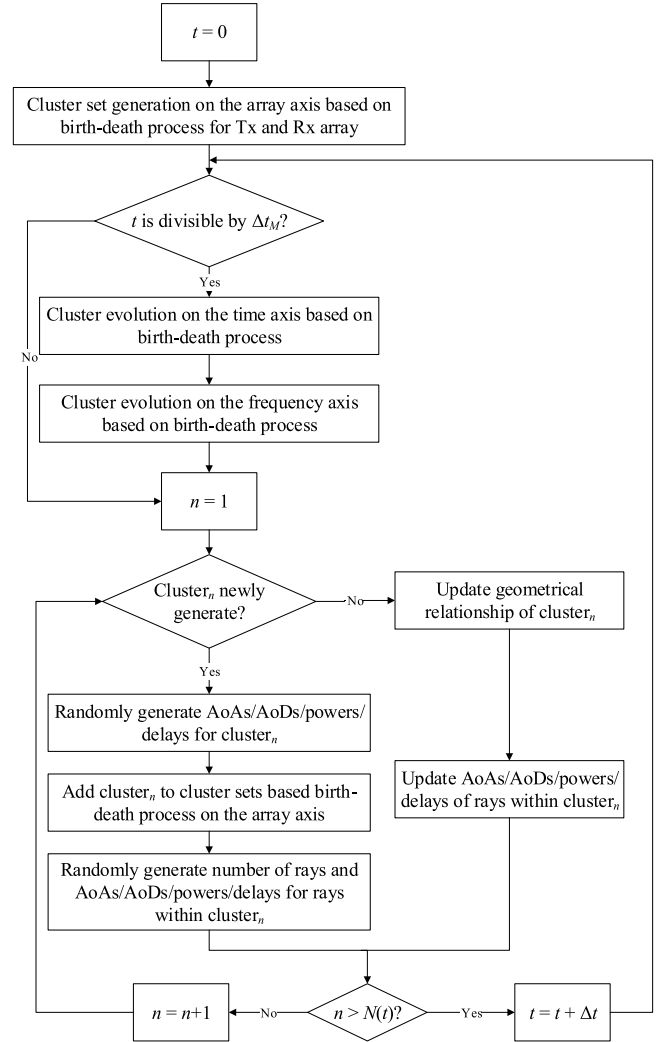


Fig. 4. Illustration of the STF cluster evolution.

cluster survival probability  $Pr(\Delta f)$  over two adjacent sub-channels with a frequency separation of  $\Delta f$  can be calculated as

$$Pr(\Delta f) = e^{-\lambda_R \frac{F(\Delta f)}{D_f^s}} \quad (62)$$

where  $D_f^s$  and  $F(\Delta f)$  can be determined by channel measurement.

- 3) When  $t$  is not divisible by  $\Delta t_M$ , only the update of remaining clusters occurs. The first process is the update of geometry relationships of clusters from  $t$  to  $t + \Delta t$ . Firstly, distance vectors of cluster<sub>*n*</sub> are updated as

$$\mathbf{D}_{n,m_n}^T(t + \Delta t) = \mathbf{D}_{n,m_n}^T(t) + \mathbf{v}_{n,A} \Delta t \quad (63)$$

$$\mathbf{D}_{n,m_n}^R(t + \Delta t) = \mathbf{D}_{n,m_n}^R(t) + \mathbf{v}_{n,Z} \Delta t - \mathbf{v}_{R,x} \Delta t \quad (64)$$

Then the corresponding updated delay of cluster<sub>*n*</sub> can be expressed as

$$\begin{aligned} \tau_{n,m_n}(t + \Delta t) &= \frac{\|\mathbf{D}_{n,m_n}^T(t + \Delta t)\| + \|\mathbf{D}_{n,m_n}^R(t + \Delta t)\|}{c} \\ &\quad + \tilde{\tau}_{n,m_n}(t + \Delta t) \end{aligned} \quad (65)$$

where the virtual link delay  $\tilde{\tau}_{n,m_n}(t + \Delta t)$  at time  $t + \Delta t$  can be calculated as the first-order filtering of  $\tilde{\tau}_{n,m_n}(t)$  and expressed as

$$\tilde{\tau}_{n,m_n}(t + \Delta t) = e^{-\frac{\Delta t}{\varsigma}} \tilde{\tau}_{n,m_n}(t) + \left(1 - e^{-\frac{\Delta t}{\varsigma}}\right) \Upsilon. \quad (66)$$

Here,  $\Upsilon$  is a random variable independent to  $\tilde{\tau}_{n,m_n}$ , but identically distributed as  $\tilde{\tau}_{n,m_n}$ , and  $\varsigma$  is a scenario-dependent parameter describing the coherence of virtual links.

### III. DERIVATIONS OF CHANNEL STATISTICAL PROPERTIES

In this section, the derivation of STFCE and its deductions, delay PSD, and Doppler PSD of the proposed novel shortwave channel model are given. In addition, the channel capacity and singular value spread (SVS) for the proposed model are also presented.

#### A. The STFCE

The STFCE calculates the correlation for channel gain between different antenna pairs and can be defined as (67), shown at the bottom of the next page, where  $\mathbb{E}[\cdot]$  denotes expectation operation and  $(\cdot)^*$  denotes the complex conjugate operation.

#### B. The Space Cross-Correlation Function (SCCF)

The SCCF is the deduction of the STFCE, reflecting relevant characteristics of the channel in the space domain. Since massive MIMO antenna arrays are different from traditional smaller antenna arrays, correlations between antennas are very important characteristics to be investigated directly. The SCCF can be derived as (68), shown at the bottom of the next page, by setting  $\Delta t = 0$  and  $\Delta f = 0$  in STFCE.

#### C. The Time Autocorrelation Function (TACF)

The TACF reflects correlation characteristics of the channel in the time domain. Considering the mobility of the transceiver and scatterer, the non-stationarity of the channel in the time domain needs to be considered. Such non-stationarity can be observed by the change trend of the TACF at different moments. We can derive the TACF as (69), shown at the bottom of the next page, by letting  $q = q', p = p'$ , and  $\Delta f = 0$  in STFCE.

#### D. The Frequency Correlation Function (FCF)

The FCF reflects the correlation of the channel in the frequency domain. By calculating the FCF, we can observe whether the correlation characteristics of both models are consistent in the frequency domain. In addition, we can obtain important channel parameters such as the correlation frequency. We can derive the FCF as (70), shown at the bottom of the next page, by setting  $q = q', p = p'$ , and  $\Delta t = 0$  in STFCE.

#### E. Delay PSD and Delay Spread

The delay PSD for the  $p$ -th Tx antenna and  $q$ -th Rx antenna is represented by

$$\Phi_{qp}(t, \tau) = \sum_{n=1}^{N_{qp}(t)} \sum_{m_n=1}^{M_n} |h_{qp,m_n}(t)|^2 \delta(\tau - \tau_{qp,m_n}(t)). \quad (71)$$

Mean powers and delays of rays within clusters will affect the time-variant delay PSD. The delay spread determines whether adaptive equalization is adopted at Rx side. If the delay spread exceeds 10 to 20 percent of the symbol duration, then adaptive equalization will be required. The delay spread  $\vartheta_\tau(t)$  is calculated as

$$\vartheta_\tau(t) = \left[ \frac{\sum_{n=1}^{N_{qp}(t)} \sum_{m_n=1}^{M_n} (\tau_{qp,m_n}(t) - \nu_\tau)^2 \Phi_{qp}(t, \tau)}{\sum_{n=1}^{N_{qp}(t)} \sum_{m_n=1}^{M_n} \Phi_{qp}(t, \tau)} \right]^{1/2}. \quad (72)$$

Here, the average delay  $\nu_\tau$  of the channel model is denoted as

$$\nu_\tau = \frac{\sum_{n=1}^{N_{qp}(t)} \sum_{m_n=1}^{M_n} \tau_{qp,m_n}(t) \Phi_{qp}(t, \tau)}{\sum_{n=1}^{N_{qp}(t)} \sum_{m_n=1}^{M_n} \Phi_{qp}(t, \tau)}. \quad (73)$$

#### F. Doppler PSD

The Doppler PSD gives the average power at the channel output as a function of Doppler frequency. It can be viewed as the scattering function averaged over all time delays and calculated by the Fourier transform of the TACF with respect to  $\Delta t$ . The Doppler PSD  $\Pi_{qp}(f, t)$  is denoted as

$$\Pi_{qp}(f, t) = \int_{-\infty}^{\infty} R_{qp}(t, f; \Delta t) e^{-j2\pi f \Delta t} d\Delta t. \quad (74)$$

#### G. SVS

The channel matrix can be expressed as singular value decomposition (SVD)

$$\mathbf{H} = \mathbf{U} \mathbf{\Sigma} \mathbf{V} \quad (75)$$

where  $\mathbf{U}$  is an  $M_R \times M_R$  unitary matrix,  $\mathbf{V}$  is an  $M_T \times M_T$  unitary matrix, and  $\mathbf{\Sigma}$  is an  $M_R \times M_T$  matrix. Furthermore, the SVS  $\zeta$  can be calculated as

$$\zeta = \frac{\max_i \sigma_i}{\min_i \sigma_i} \quad (76)$$

where  $\sigma_i$  ( $i = 1, 2, \dots, I$ ) is the singular value of  $\mathbf{H}$  and  $I$  is the smaller one of  $M_R$  and  $M_T$ .

### H. Channel Capacity

As one of the key indicators for communication systems, the channel capacity reflects link-level (single user), or even system-level (multi-user) performance for channel models. For the validation of channel models, not only cluster-level analysis and validation are needed, but also from the perspective of the whole system. The average channel capacity with uniform Tx power allocation can be calculated as

$$C = \mathbb{E} \left\{ \log_2 \det \left( \mathbf{I} + \frac{\text{SNR}}{M_T} \bar{\mathbf{H}} \bar{\mathbf{H}}^H \right) \right\} \quad (77)$$

where  $\det(\cdot)$  denotes the determinant operation,  $\mathbf{I}$  is the  $M_R \times M_R$  identity matrix, SNR denotes the signal-to-noise ratio, and  $\bar{\mathbf{H}}$  is the normalized channel matrix and can be obtained as

$$\bar{\mathbf{H}} = \mathbf{H} \cdot \left\{ \frac{1}{M_T M_R} \sum_{k,l} |h_{k,l}|^2 \right\}^{-\frac{1}{2}}. \quad (78)$$

## IV. RESULTS AND ANALYSIS

In this section, we provide simulation results and corresponding analyses to show statistical properties of the proposed shortwave massive MIMO channel model. Parameters in the model simulations, including the Tx/Rx heights, antenna separations, carrier frequencies, and motion velocities, were set according to the relevant ITU handbook [46] and corresponding measurements. For example, the parameters used for our simulations here were set as:  $h_T = 30$  m,  $h_R = 2.5$  m,  $\beta_A^T = \pi/6$ ,  $\beta_E^T = 0$ ,  $\sigma_{DS} = 7$  m,  $\sigma_{AS} = 12$  m, and,  $\sigma_{ES} = 8$  m. Antenna arrays at both the Tx and Rx are assumed to have a spacing of  $\delta_T = \delta_R = \lambda/2$ . Other parameters were determined by fitting statistical properties to those of the analytical model.

Simulations of SCCFs at different carrier frequencies are shown in Fig. 4. When simulating SCCF, we often set the number of antennas at one side as 1, and then study the correlation between antennas at the other side. In this simulation, we set the number of Rx antennas as 1 and the number of Tx antennas as 128. The transceiver remain stationary. It can be seen that the theoretical model fit well with the simulation results. The higher the working frequency, the faster the SCCF decreases. The change of working frequency will bring about the change of spatial correlation.

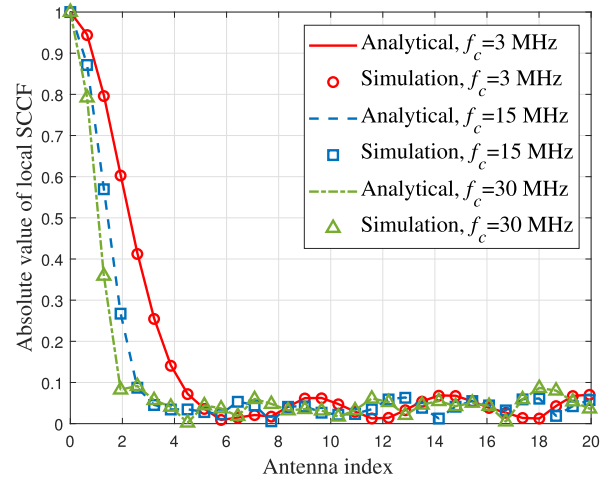


Fig. 5. Analytical and simulated local SCCFs of the proposed short-wave channel model at different frequencies ( $M_T = 128$ ,  $M_R = 1$ ,  $t = 1$  s,  $\delta_T = \lambda/2$ ,  $\beta_A^T = \pi/6$ ,  $\beta_E^T = 0$ ,  $v^T = 0$  m/s,  $v^R = 0$  m/s,  $\sigma_{DS} = 0.5$  ms,  $\sigma_{AS} = 12$  m, and  $\sigma_{ES} = 8$  m).

Fig. 6 shows the variation curve of simulated TACF at different carrier frequencies. It can be seen that the theoretical model is in good agreement with the simulation results. The TACF decreases faster with the increase of the carrier frequency. With the increase of carrier frequency, the delay spread will increase, while the angular spreads, coherence time, and Doppler PSD will decrease. In addition, the higher carrier frequency will induce a larger phase shift. The composite effect leads to the decrease of TACF as the carrier frequency increases, which is in agreement with the simulation results in [44] and [47]. Above results prove the accuracy of the proposed channel model. It is very important to select appropriate working frequency for shortwave communication systems.

Fig. 7 simulates FCFs at different correlation frequencies. The smaller the correlation frequency is, the faster the FCF decreases. In parameter setting, an appropriate value of the correlation frequency should be selected to ensure the frequency correlation of the channel.

To verify the correctness of the path loss model, we compare simulation results with that of the measurement data. We select results of [48] with a working frequency of 15 MHz for comparison and set corresponding model parameters according to [48]. The proposed channel model is fitted with the

$$\begin{aligned} R_{qp,q'p'}(t, f; \Delta t, \Delta f, \delta_T, \delta_R) &= \mathbb{E} [h_{qp}(t, f) h_{q'p'}^*(t + \Delta t, f + \Delta f)] = R_{qp,q'p'}^G(t, f; \Delta t, \Delta f, \delta_T, \delta_R) \cdot \varepsilon(D_{\max}^G - D) \\ &+ R_{qp,q'p'}^N(t, f; \Delta t, \Delta f, \delta_T, \delta_R) \cdot \varepsilon(D - D_{\max}^G) \cdot \varepsilon(D_{\min}^S - D) \\ &+ R_{qp,q'p'}^S(t, f; \Delta t, \Delta f, \delta_T, \delta_R) \cdot \varepsilon(D - D_{\min}^S). \end{aligned} \quad (67)$$

$$\begin{aligned} R_{qp,q'p'}(t, f; \delta_T, \delta_R) &= \mathbb{E} [h_{qp}(t, f) h_{q'p'}^*(t, f)] = R_{qp,q'p'}^G(t, f; \delta_T, \delta_R) \cdot \varepsilon(D_{\max}^G - D) + R_{qp,q'p'}^N(t, f; \delta_T, \delta_R) \\ &\times \varepsilon(D - D_{\max}^G) \cdot \varepsilon(D_{\min}^S - D) + R_{qp,q'p'}^S(t, f; \delta_T, \delta_R) \cdot \varepsilon(D - D_{\min}^S). \end{aligned} \quad (68)$$

$$\begin{aligned} R_{qp}(t, f; \Delta t) &= \mathbb{E} [h_{qp}(t, f) h_{qp}^*(t + \Delta t, f)] = R_{qp}^G(t, f; \Delta t) \cdot \varepsilon(D_{\max}^G - D) + R_{qp}^N(t, f; \Delta t) \cdot \varepsilon(D - D_{\max}^G) \\ &\times \varepsilon(D_{\min}^S - D) + R_{qp}^S(t, f; \Delta t) \cdot \varepsilon(D - D_{\min}^S). \end{aligned} \quad (69)$$

$$\begin{aligned} R_{qp}(t, f; \Delta f) &= \mathbb{E} [h_{qp}(t, f) h_{qp}^*(t, f + \Delta f)] = R_{qp}^G(t, f; \Delta f) \cdot \varepsilon(D_{\max}^G - D) + R_{qp}^N(t, f; \Delta f) \cdot \varepsilon(D - D_{\max}^G) \\ &\times \varepsilon(D_{\min}^S - D) + R_{qp}^S(t, f; \Delta f) \cdot \varepsilon(D - D_{\min}^S). \end{aligned} \quad (70)$$

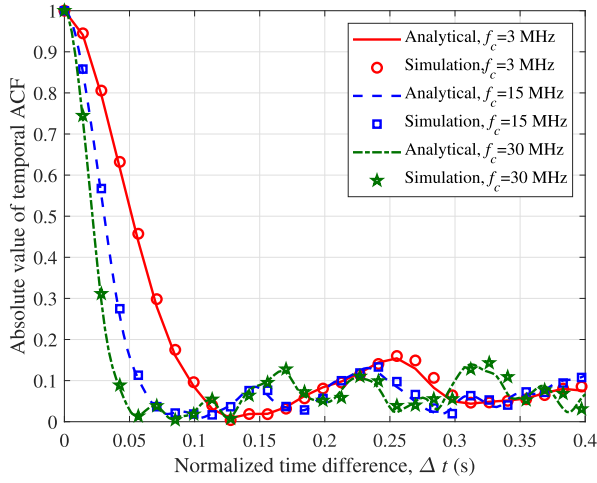


Fig. 6. Analytical and simulated local TACFs of the proposed shortwave channel model at different frequencies ( $M_T = 128, M_R = 1, t = 1$  s,  $\delta_T = \lambda/2, \beta_A^T = \pi/6, \beta_E^T = 0, v^T = 0$  m/s,  $v^R = 0$  m/s,  $\sigma_{DS} = 0.5$  ms,  $\sigma_{AS} = 12$  m, and  $\sigma_{ES} = 8$  m).

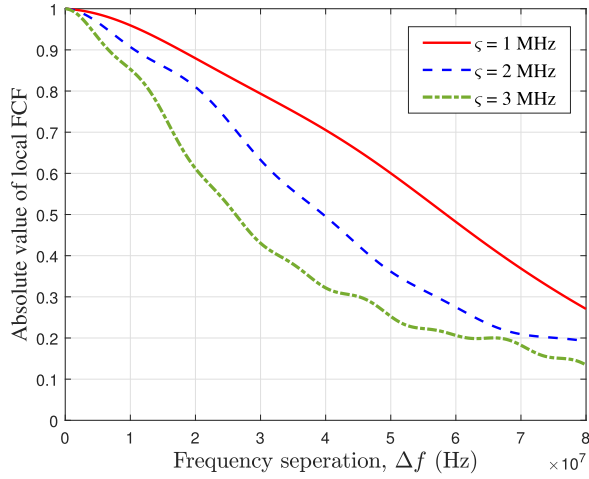


Fig. 7. Simulated FCFs of the proposed shortwave channel model at different correlation frequencies ( $M_T = 128, M_R = 1, t = 1$  s,  $f_c = 20$  MHz,  $\delta_T = \lambda/2, \beta_A^T = \pi/6, \beta_E^T = 0, v^T = 0$  m/s,  $v^R = 0$  m/s,  $\sigma_{DS} = 0.5$  ms,  $\sigma_{AS} = 12$  m, and  $\sigma_{ES} = 8$  m).

measurement data according to the minimum mean square error (MMSE) criterion for parameters not involved in the literature. Fig. 8 shows simulation results of path loss in the groundwave at different carrier frequencies. Fig. 9 shows simulation results of path loss in the skywave case at different carrier frequencies. It can be seen that the proposed channel model is in good agreement with the measurement data, which proves the accuracy of the model. As can be seen from figures, the path loss increases with the distance and working frequency.

The normalized delay PSD for the linear motion of Rx is given in Fig. 10. We set the delay spread as 5 ms in the simulations. It can be seen that as the position of Rx changes, the corresponding time delay is also shifted. From the color of delay PSD, the lighter the color is, the higher the corresponding power is. We can see a distinct line with the lightest color representing the main path of the shortwave channel. The normalized Doppler PSD corresponding to different time

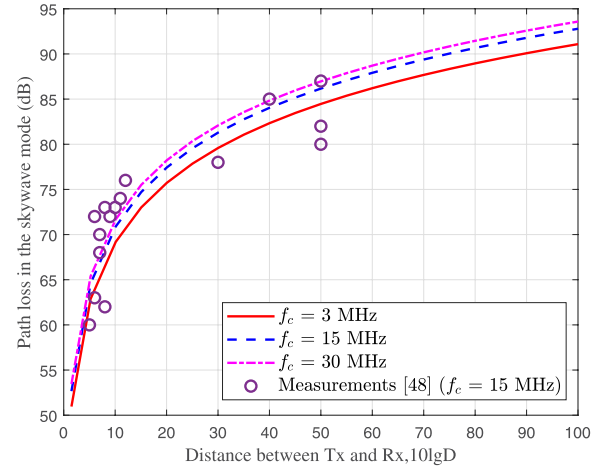


Fig. 8. Path losses of the proposed shortwave channel model at different frequencies in the skywave mode ( $M_T = 1, M_R = 1, h_T = 30$  m, and  $h_R = 2.5$  m).

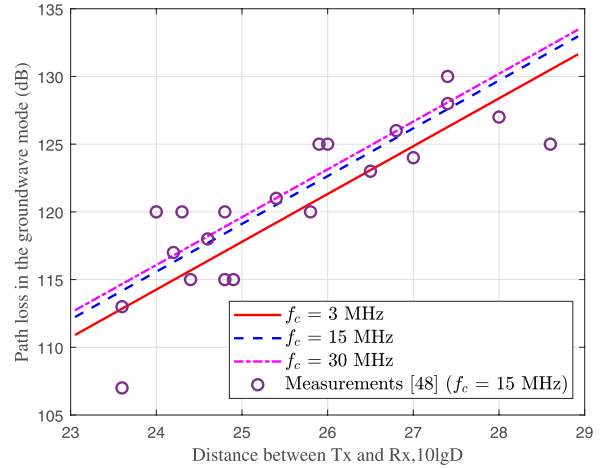


Fig. 9. Path losses of the proposed shortwave channel model at different frequencies in the groundwave mode ( $M_T = 1, M_R = 1, h_T = 30$  m, and  $h_R = 2.5$  m).

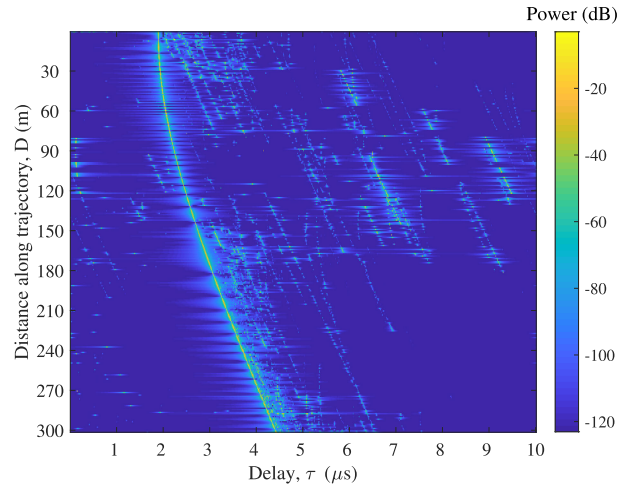


Fig. 10. Delay PSDs of the proposed shortwave channel model ( $M_T = 128, M_R = 1, \delta_T = \lambda/2, \beta_A^T = \pi/6, \beta_E^T = 0, \sigma_{DS} = 0.5$  ms,  $\sigma_{AS} = 12$  m, and  $\sigma_{ES} = 8$  m).

instants  $t = 0, 3,$  and  $6$  s at carrier frequency  $f_c = 15$  MHz is shown in Fig. 11. The corresponding Doppler PSD varies from moment to moment, proving the temporal non-stationarity. The

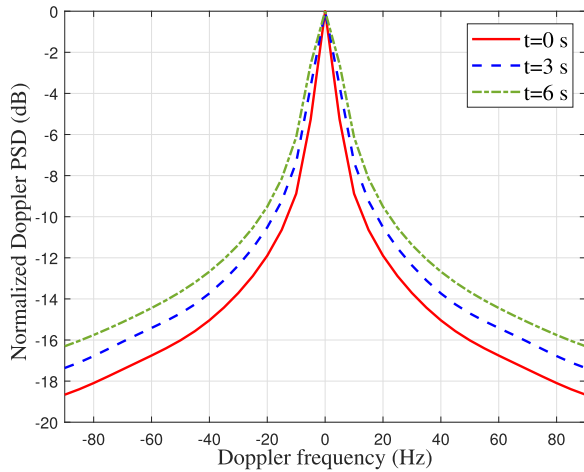


Fig. 11. Doppler PSDs of the proposed shortwave channel model at different times ( $M_T = 128$ ,  $M_R = 1$ ,  $\delta_T = \lambda/2$ ,  $\beta_A^T = \pi/6$ ,  $\beta_E^T = 0$ ,  $\sigma_{DS} = 0.5$  ms,  $\sigma_{AS} = 12$  m, and  $\sigma_{ES} = 8$  m).

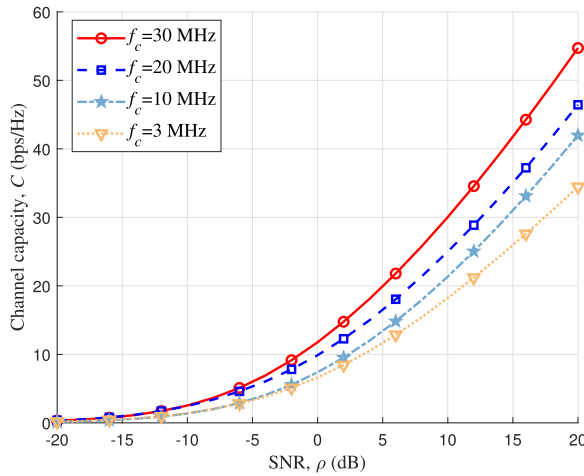


Fig. 12. Channel capacities of the proposed shortwave channel model at different frequencies ( $M_T = 128$ ,  $M_R = 1$ ,  $t = 1$  s,  $\delta_T = \lambda/2$ ,  $\beta_A^T = \pi/6$ ,  $\beta_E^T = 0$ ,  $\sigma_{DS} = 0.5$  ms,  $\sigma_{AS} = 12$  m, and  $\sigma_{ES} = 8$  m).

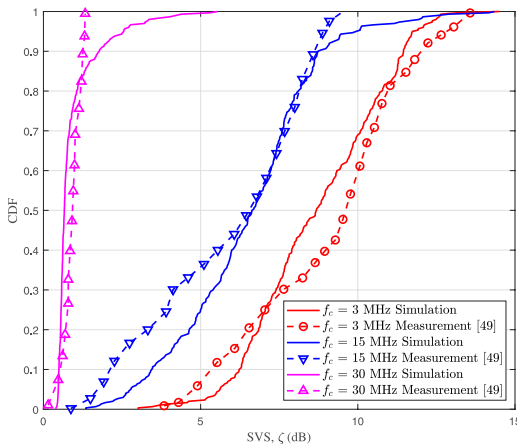


Fig. 13. Comparisons of SVSs between the proposed shortwave channel model and measurements ( $M_T = 128$ ,  $M_R = 1$ ,  $t = 1$  s,  $\delta_T = \lambda/2$ ,  $\beta_A^T = \pi/6$ ,  $\beta_E^T = 0$ ,  $\sigma_{DS} = 0.5$  ms,  $\sigma_{AS} = 12$  m, and  $\sigma_{ES} = 8$  m).

channel capacity reflects the maximum amount of information that the channel can transmit without error. Fig. 12 shows

the relationship between channel capacity and SNR. As the SNR increases, channel capacity also increases. In addition, the increase of working frequency will also bring increase of channel capacity. However, the increase of working frequency will bring the increase of loss. Therefore, the choice of shortwave working frequency should consider the compromise between channel model performance and loss cost.

Cumulative distribution functions (CDFs) of SVS corresponding to different carrier frequencies are presented in Fig. 13. As can be seen from the figure, the SVS decreases with decreasing frequency. Simulation results fit well with measurement results [49] by optimizing model parameters. It proves the accuracy of the proposed channel model.

## V. CONCLUSION

A novel 3D non-stationary massive MIMO GBSM for shortwave communication systems has been proposed in this paper. Three shortwave transmission modes, i.e., the ground-wave, NVIS, and long-distance skywave modes, have been combined to eliminate the communication blind area between long-distance skywave and groundwave. Therefore, the full coverage of shortwave transmission in long-distance communications can be guaranteed. The ionospheric absorption loss and surface reflection loss during multi-hop transmission have been employed in the proposed channel model. In addition, the near-field spherical wavefront effect and STF non-stationarities have been considered. Channel statistical properties have been simulated and analyzed. Simulation results have verified the STF non-stationarities of the proposed channel model and the accuracy has been demonstrated by comparing simulations with measurement data. Results have shown that ST correlations and channel capacities decrease with the decreasing working frequency. Therefore, the working frequency of shortwave communication systems has a direct impact on channel characteristics and system performances. It is necessary to predict the OWF in advance according to actual environments. The proposed non-stationary massive MIMO shortwave channel model will provide a theoretical basis for the design and construction of future massive MIMO shortwave communication systems.

## REFERENCES

- [1] F. H. Raab et al., "HF, VHF, and UHF systems and technology," *IEEE Trans. Microw. Theory Techn.*, vol. 50, no. 3, pp. 888–899, Mar. 2002.
- [2] T. L. Marzetta, E. G. Larsson, H. Yang, and H. Q. Ngo, *Fundamentals of Massive MIMO*. Cambridge, U.K.: Cambridge Univ. Press, 2016.
- [3] C.-X. Wang et al., "On the road to 6G: Visions, requirements, key technologies and testbeds," *IEEE Commun. Surveys Tuts.*, vol. 25, no. 2, pp. 905–974, 2nd Quart. 2023.
- [4] X. You et al., "Towards 6G wireless communication networks: Vision, enabling technologies, and new paradigm shifts," *Sci. China Inf. Sci.*, vol. 64, no. 1, Nov. 2020, Art. no. 110301.
- [5] Y. Zheng et al., "Ultra-massive MIMO channel measurements at 5.3 GHz and a general 6G channel model," *IEEE Trans. Veh. Technol.*, vol. 72, no. 1, pp. 20–34, Jan. 2023.
- [6] C. F. López, C.-X. Wang, and Y. Zheng, "A 3D non-stationary wideband massive MIMO channel model based on ray-level evolution," *IEEE Trans. Commun.*, vol. 70, no. 1, pp. 621–634, Jan. 2022.
- [7] X. Yu, A.-A. Lu, X. Gao, G. Y. Li, G. Ding, and C.-X. Wang, "HF skywave massive MIMO communication," *IEEE Trans. Wireless Commun.*, vol. 21, no. 4, pp. 2769–2785, Apr. 2022.

- [8] G. J. Frazer, "Experimental results for MIMO methods applied in over-the-horizon radar," *IEEE Aerosp. Electron. Syst. Mag.*, vol. 32, no. 12, pp. 52–69, Dec. 2017.
- [9] F. Orga, M. Hervás, and R. M. Alsina-Pages, "Flexible low-cost SDR platform for HF communications: Near vertical incidence skywave preliminary results," *IEEE Antennas Propag. Mag.*, vol. 58, no. 6, pp. 49–56, Dec. 2016.
- [10] M. Uysal and M. R. Heidarpour, "Cooperative communication techniques for future-generation HF radios," *IEEE Commun. Mag.*, vol. 50, no. 10, pp. 56–63, Oct. 2012.
- [11] C.-X. Wang, J. Huang, H. Wang, X. Gao, X. You, and Y. Hao, "6G wireless channel measurements and models: Trends and challenges," *IEEE Veh. Technol. Mag.*, vol. 15, no. 4, pp. 22–32, Dec. 2020.
- [12] H. Jiang, M. Mukherjee, J. Zhou, and J. Lloret, "Channel modeling and characteristics for 6G wireless communications," *IEEE Netw.*, vol. 35, no. 1, pp. 296–303, Jan./Feb. 2021.
- [13] C. Watterson, J. Juroshek, and W. Bensema, "Experimental confirmation of an HF channel model," *IEEE Trans. Commun. Technol.*, vol. COM-18, no. 6, pp. 792–803, Dec. 1970.
- [14] M. Nesenbergs, "Modeling of wideband HF channels," DTIC Res., Fort Belvoir, VA, USA, Tech. Rep. ADP006134, 1987.
- [15] J. J. Barratt and T. L. Walton, "A real-time wideband propagation simulator for the high frequency band," in *Proc. Ionospheric Effects Symp.*, 1987, pp. 9–20.
- [16] L. Van der Perre, A. Van de Capelle, M. Ade, and R. Lauwereins, "Implementation of an extended simulator for the HF channel on a multi-DSP board," in *Proc. 7th Int. Conf. HF Radio Syst. Techn.* Nottingham, U.K., Jul. 1997, pp. 373–377.
- [17] J. D. Milsom, "Wideband channel characteristics and short spread-spectrum HF links," in *Proc. 8th Int. Conf. HF Radio Syst. Techn.* Guildford, U.K., Jul. 2000, pp. 305–309.
- [18] L. E. Vogler et al., "Progress and remaining issues in the development of a wideband HF channel model and simulator," in *Proc. AGARD*, Paris, France, Dec. 1989, pp. 1–6.
- [19] J. A. Hoffmeyer and L. E. Vogler, "A new approach to HF channel modeling and simulation," in *Proc. IEEE Conf. Mil. Commun.*, Monterey, CA, USA, Sep./Oct. 1990, pp. 1199–1208.
- [20] R. P. Basler, G. H. Price, R. T. Tsunoda, and T. L. Wong, "Ionospheric distortion of HF signals," *Radio Sci.*, vol. 23, no. 4, pp. 569–579, Jul. 1988.
- [21] J. A. Hoffmeyer, L. E. Vogler, J. F. Mastrangelo, L. E. Pratt, and C. J. Behm, "A new HF channel model and its implementation in a real-time simulator," in *Proc. 5th Int. Conf. HF Radio Syst. Techn.*, Edinburgh, U.K., Jul. 1991, pp. 173–177.
- [22] J. Mastrangelo, J. Hoffmeyer, C. Behm, and L. Pratt, "A new wideband HF simulation system for testing HF radios," in *Proc. MILCOM*, McLean, VA, USA, Nov. 1991, pp. 1156–1161.
- [23] J. J. Lemmon, "Wideband HF noise and interference modeling," in *Proc. IEEE MILCOM*, Boston, MA, USA, Oct. 1989, pp. 846–851.
- [24] J. J. Lemmon, "Model for the simulation of wideband HF noise and interference," in *Proc. 5th Int. Conf. HF Radio Syst. Techn.*, Edinburgh, U.K., Jul. 1991, pp. 349–353.
- [25] J. J. Lemmon and C. J. Behm, "Wideband HF noise/interference modeling. Part I: First-order statistics," Tech. Memorandum Ser., NASA, Washington, DC, USA, STI/Recon Tech. Rep. N91, 1991, Art. no. 32281.
- [26] J. F. Mastrangelo, J. J. Lemmon, L. E. Vogler, J. A. Hoffmeyer, L. E. Pratt, and C. J. Behm, "A new wideband high frequency channel simulation system," *IEEE Trans. Commun.*, vol. COM-45, no. 1, pp. 26–34, Jan. 1997.
- [27] J. J. Lemmon and C. J. Behm, *Wideband HF Noise/Interference Modeling. Part II: Higher-Order Statistics*. Boulder, CO, USA: ITS, 1993.
- [28] C. J. Behm, "A narrowband high frequency channel simulator with delay spread," in *Proc. 7th Int. Conf. HF Radio Syst. Techn.*, Nottingham, U.K., Jul. 1997, pp. 388–391.
- [29] M. Lecote and M. Testard, "A model of high frequencies (HF) channel used to design a modem of 9600 bits/s rate in 3 kHz of bandwidth," in *Proc. IEEE MILCOM*, Monterey, CA, USA, Nov. 1997, pp. 351–355.
- [30] S. Wu, C.-X. Wang, E.-H. M. Aggoune, M. M. Alwakeel, and Y. He, "A non-stationary 3-D wideband twin-cluster model for 5G massive MIMO channels," *IEEE J. Sel. Areas Commun.*, vol. 32, no. 6, pp. 1207–1218, Jun. 2014.
- [31] C. F. López and C.-X. Wang, "Novel 3-D non-stationary wideband models for massive MIMO channels," *IEEE Trans. Wireless Commun.*, vol. 17, no. 5, pp. 2893–2905, May 2018.
- [32] A. O. Martínez, P. Eggers, and E. D. Carvalho, "Geometry-based stochastic channel models for 5G: Extending key features for massive MIMO," in *Proc. IEEE PIMRC*, Valencia, Spain, Sep. 2016, pp. 1–6.
- [33] Y. Xie, B. Li, X. Zuo, M. Yang, and Z. Yan, "A 3D geometry-based stochastic model for 5G massive MIMO channels," in *Proc. QSHINE*, Taiwan, Aug. 2015, pp. 216–222.
- [34] T. S. Rappaport et al., "Wireless communications and applications above 100 GHz: Opportunities and challenges for 6G and beyond," *IEEE Access*, vol. 7, pp. 78729–78757, 2019, doi: 10.1109/ACCESS.2019.2921522.
- [35] *Study on Channel Model for Frequencies From 0.5 to 100 GHz (Release 14)*, document TR 38.901, 3GPP, Sophia Antipolis, France, Version 14.0.0, Mar. 2017.
- [36] V. Nurmela et al., *METIS Channel Models*, document ICT-317669/D1.4, METIS, New York, NY, USA, Jul. 2015.
- [37] X.-Y. Cao, *Antenna and Radio Wave Propagation*, Beijing, China: Publishing House of Electronics Industry, 2015.
- [38] *Definitions of Maximum and Minimum Transmission Frequencies*, document ITU-R P.373-8, ITU, Geneva, Switzerland, 2007.
- [39] *Method for the Prediction of the Performance of HF Circuits*, document ITU-R P.533-14, ITU, Geneva, Switzerland, 2019.
- [40] *ITU-R Methods of Basic MUF, Operational MUF and Ray-Path Prediction*, document ITU-R P.1240-7, ITU, Geneva, Switzerland, 2019.
- [41] M. Hata, "Empirical formula for propagation loss in land mobile radio services," *IEEE Trans. Veh. Technol.*, vol. VT-29, no. 3, pp. 317–325, Aug. 1980.
- [42] L. Man, "Range air-ground HF communication based on channel characteristic analysis," *Telecommun. Eng.*, vol. 52, no. 9, pp. 1508–1512, Mar. 2013.
- [43] *Propagation Effects Relating to Terrestrial Land Mobile Service in the VHF and UHF Bands*, document ITU-R P.1406-2, ITU, Geneva, Switzerland, Jul. 2015.
- [44] J. Bian, C.-X. Wang, X. Gao, X. You, and M. Zhang, "A general 3D non-stationary wireless channel model for 5G and beyond," *IEEE Trans. Wireless Commun.*, vol. 20, no. 5, pp. 3211–3224, May 2021.
- [45] C.-X. Wang, Z. Lv, X. Gao, X. You, Y. Hao, and H. Haas, "Pervasive wireless channel modeling theory and applications to 6G GBsMs for all frequency bands and all scenarios," *IEEE Trans. Veh. Technol.*, vol. 71, no. 9, pp. 9159–9173, Sep. 2022.
- [46] *Handbook: The Ionosphere and Its Effects on Radiowave Propagation*, Radiocomm. Bur., ITU, Geneva, Switzerland, 1998.
- [47] H. Chang et al., "A novel nonstationary 6G UAV-to-ground wireless channel model with 3-D arbitrary trajectory changes," *IEEE Internet Things J.*, vol. 8, no. 12, pp. 9865–9877, Jun. 2021.
- [48] *Ground-Wave Propagation Curves for Frequencies Between 10 kHz and 30 MHz*, document ITU-R P.368-9, ITU, Geneva, Switzerland, Feb. 2007.
- [49] *Sky-Wave Field Strength Prediction Method for Propagation to Aircraft at About 500 kHz*, document ITU-R P.683-0, ITU, Geneva, Switzerland, Jan. 1990.



**Fan Lai** (Student Member, IEEE) received the B.E. degree from Dalian Maritime University, Dalian, China, in 2015. He is currently pursuing the Ph.D. degree with the National Mobile Communications Research Laboratory, Southeast University, Nanjing, China. His research interests include massive MIMO channel measurements and modeling and shortwave channel modeling.



**Cheng-Xiang Wang** (Fellow, IEEE) received the B.Sc. and M.Eng. degrees in communication and information systems from Shandong University, China, in 1997 and 2000, respectively, and the Ph.D. degree in wireless communications from Aalborg University, Denmark, in 2004.

He was a Research Assistant with the Hamburg University of Technology, Hamburg, Germany, from 2000 to 2001, a Visiting Researcher with Siemens AG Mobile Phones, Munich, Germany, in 2004, and a Research Fellow with the University of Agder, Grimstad, Norway, from 2001 to 2005. He has been with Heriot-Watt University, Edinburgh, U.K., since 2005, where he was promoted to a Professor in 2011. In 2018, he joined Southeast University, Nanjing, China, as a Professor. He is currently a part-time Professor with Purple Mountain Laboratories, Nanjing. He has authored four books, three book chapters, and more than 500 papers in refereed journals and conference proceedings, including 27 highly cited papers. He has also delivered 24 invited keynote speeches/talks and 16 tutorials in international conferences. His current research interests include wireless channel measurements and modeling, 6G wireless communication networks, and electromagnetic information theory.

Dr. Wang is a member of the Academia Europaea (The Academy of Europe), a member of the European Academy of Sciences and Arts (EASA), a fellow of the Royal Society of Edinburgh (FRSE), IET, and the China Institute of Communications (CIC), an IEEE Communications Society Distinguished Lecturer in 2019 and 2020, and a Highly-Cited Researcher recognized by Clarivate Analytics during 2017–2020. He is also an Executive Editorial Committee Member of the IEEE TRANSACTIONS ON WIRELESS COMMUNICATIONS. He has served as a TPC member, the TPC chair, and the general chair for more than 30 international conferences. He received 15 best paper awards from IEEE GLOBECOM 2010, IEEE ICCT 2011, ITST 2012, IEEE VTC 2013 Spring, IWCMC 2015, IWCMC 2016, IEEE/CIC ICC 2016, WPMC 2016, WOCC 2019, IWCMC 2020, WCSP 2020, CSPS2021, WCSP 2021, and IEEE/CIC ICC 2022. He has served as the Editor for over ten international journals, including the IEEE TRANSACTIONS ON WIRELESS COMMUNICATIONS from 2007 to 2009, the IEEE TRANSACTIONS ON VEHICULAR TECHNOLOGY from 2011 to 2017, and the IEEE TRANSACTIONS ON COMMUNICATIONS from 2015 to 2017. He was the Guest Editor of the IEEE JOURNAL ON SELECTED AREAS IN COMMUNICATIONS, Special Issue on Vehicular Communications and Networks (Lead Guest Editor), Special Issue on Spectrum and Energy Efficient Design of Wireless Communication Networks, and Special Issue on Airborne Communication Networks. He was also the Guest Editor of the IEEE TRANSACTIONS ON BIG DATA, Special Issue on Wireless Big Data, and is a Guest Editor for the IEEE TRANSACTIONS ON COGNITIVE COMMUNICATIONS AND NETWORKING, Special Issue on Intelligent Resource Management for 5G and Beyond.



**Jie Huang** (Member, IEEE) received the B.E. degree in information engineering from Xidian University, China, in 2013, and the Ph.D. degree in information and communication engineering from Shandong University, China, in 2018. From October 2018 to October 2020, he was a Post-Doctoral Research Associate with the National Mobile Communications Research Laboratory, Southeast University, China, supported by the National Postdoctoral Program for Innovative Talents. From January 2019 to February 2020, he was a Post-Doctoral Research

Associate with Durham University, U.K. Since March 2019, he has been a part-time Researcher with Purple Mountain Laboratories, China. Since November 2020, he has been an Associate Professor with the National Mobile Communications Research Laboratory, Southeast University. He has authored or coauthored more than 70 papers in refereed journals and conference proceedings. His research interests include millimeter wave, massive MIMO, reconfigurable intelligent surface channel measurements and modeling, wireless big data, and 6G wireless communications. He received the Best Paper Award from WPMC 2016, WCSP 2020, and WCSP 2021. He has delivered nine tutorials in IEEE/CIC ICC 2021, IEEE PIMRC 2021, IEEE ICC 2022, IEEE VTC Spring 2022, IEEE/CIC ICC 2022, IEEE VTC-Fall 2022, IEEE PIMRC 2022, IEEE GLOBECOM 2022, and IEEE WCNC 2023.



**Rui Feng** received the B.Sc. degree in communication engineering and the M.Eng. degree in signal and information processing from Yantai University, China, in 2011 and 2014, respectively, and the Ph.D. degree in communication and information system from Shandong University, China, in 2018. From July 2018 to September 2020, she was a Lecturer with Ludong University, China. She is currently a Post-Doctoral Research Associate with Purple Mountain Laboratories and Southeast University, China. Her research interests include (ultra-) massive

MIMO channel modeling theory and beam domain channel modeling.



**Xiqi Gao** (Fellow, IEEE) received the Ph.D. degree in electrical engineering from Southeast University, Nanjing, China, in 1997.

In April 1992, he joined the Department of Radio Engineering, Southeast University. From September 1999 to August 2000, he was a Visiting Scholar with the Massachusetts Institute of Technology, Cambridge, MA, USA, and Boston University, Boston, MA, USA. Since May 2001, he has been a Professor of information systems and communications. From August 2007 to July 2008, he visited the Darmstadt University of Technology, Darmstadt, Germany, as a Humboldt Scholar. His current research interests include broadband multicarrier communications, MIMO wireless communications, channel estimation and turbo equalization, and multirate signal processing for wireless communications.

Dr. Gao was a recipient of the Science and Technology Awards of the State Education Ministry of China in 1998, 2006, and 2009, the National Technological Invention Award of China in 2011, and the 2011 IEEE Communications Society Stephen O. Rice Prize Paper Award in the field of communication theory. From 2007 to 2012, he was the Editor of IEEE TRANSACTIONS ON WIRELESS COMMUNICATIONS. From 2009 to 2013, he was the Editor of IEEE TRANSACTIONS ON SIGNAL PROCESSING. From 2015 to 2017, he was the Editor of IEEE TRANSACTIONS ON COMMUNICATIONS.



**Fu-Chun Zheng** (Senior Member, IEEE) received the B.Eng. and M.Eng. degrees in radio engineering from the Harbin Institute of Technology, China, in 1985 and 1988, respectively, and the Ph.D. degree in electrical engineering from The University of Edinburgh, U.K., in 1992.

From 1992 to 1995, he was a Post-Doctoral Research Associate with the University of Bradford, U.K. From May 1995 to August 2007, he was with Victoria University, Melbourne, Australia, first as a Lecturer and then as an Associate Professor of mobile communications. He was a Professor (Chair) of signal processing with the University of Reading, U.K., from September 2007 to July 2016. He has been a Distinguished Adjunct Professor with Southeast University, China, since 2010. Since August 2016, he has been with the Harbin Institute of Technology (Shenzhen), China, as a Distinguished Professor. He has been awarded two U.K. EPSRC Visiting Fellowships both hosted by the University of York, U.K., first in August 2002 and then again in August 2006. Over the past two decades, he has also carried out many government and industry sponsored research projects in Australia, the U.K., and China. He was a short-term Visiting Fellow and a long-term Visiting Research Fellow with British Telecom, U.K. His current research interests include ultradense networks (UDN), ultra-reliable low latency communications (URLLC), multiple antenna systems, green communications, and machine learning-based communications.

Dr. Zheng served as the General Chair for IEEE VTC 2006-S, Melbourne, Australia, the first ever VTC held in the southern hemisphere in VTC's history of six decades, in 2006. He was the Executive TPC Chair of IEEE VTC 2016-S, Nanjing, China, the first ever VTC held in mainland China. He has served as the Lead TPC Chair for IEEE VTC 2022-F (London and Beijing). He was an Editor (2001–2004) of IEEE TRANSACTIONS ON WIRELESS COMMUNICATIONS.